

# Laboratory Investigation of the Active Nitridation of Graphite by Atomic Nitrogen

Luning Zhang,\* Dušan A. Pejaković,† and Jochen Marschall‡

*SRI International, Menlo Park, California 94025*

and

Max Dougherty§ and Douglas G. Fletcher¶

*University of Vermont, Burlington, Vermont 05405*

DOI: 10.2514/1.T3612

The reaction efficiency for the active nitridation of graphite by atomic nitrogen was investigated using a furnace-heated quartz flow tube coupled to a microwave discharge. Experiments were performed in N/N<sub>2</sub> mixtures with gas pressures ranging from about 130 to 670 Pa and furnace temperatures from 873 to 1373 K. The N-atom concentrations entering and exiting the furnace were measured by chemical titration via the N + NO → N<sub>2</sub> + O reaction, and the atom concentration at the graphite sample location was determined by interpolation, using a simple reactive-flow model. The reaction efficiency for graphite nitridation was derived from the interpolated N-atom concentration and the measured graphite mass loss for a given test time. The reaction efficiency, defined as the fraction of N-atom collisions with the surface that result in the title reaction, was found to increase from ~0.2 × 10<sup>-3</sup> at 873 K to ~9.8 × 10<sup>-3</sup> at 1373 K

## Nomenclature

$A$	= surface area, m <sup>2</sup>
$C$	= concentration, mol m <sup>-3</sup>
$D$	= diffusion coefficient, m <sup>2</sup> s <sup>-1</sup>
$D_a$	= tube surface Damköhler number, $\gamma\bar{v}d/4D$
$d$	= tube diameter, m
$d_s$	= sample diameter, m
$K_{eq}$	= equilibrium constant
$k_f, k_b$	= forward and backward surface reaction-rate constants, ms <sup>-1</sup>
$L$	= distance between titration ports, m
$L_e$	= entrance length, $0.06d Re$ , m
$L_s$	= sample length, m or mm
$M$	= molar mass, kg mol <sup>-1</sup>
$m$	= mass, kg
$\dot{m}$	= mass flow rate, kg s <sup>-1</sup>
$P$	= pressure, Pa
$R$	= universal gas constant, 8.3145 J mol <sup>-1</sup> K <sup>-1</sup>
$Re$	= tube Reynolds number, $\rho v d / \mu$
$Sc$	= Schmidt number, $\mu / \rho D$
$T$	= temperature, K
$t$	= time, s or min

$U$	= axial N-atom flux, mol m <sup>-2</sup> s <sup>-1</sup>
$v$	= bulk flow velocity, ms <sup>-1</sup>
$\bar{v}$	= average thermal speed, $\sqrt{8RT/\pi M}$ , ms <sup>-1</sup>
$x$	= sample axial coordinate, m
$z$	= flow tube axial coordinate, m
$\Delta m$	= mass change, mg
$\Delta t$	= test time, min
$\gamma$	= reaction efficiency
$\mu$	= viscosity, Pa s
$\rho$	= density, kg m <sup>-3</sup>
$\chi$	= mole fraction

## Subscripts

ave	= average
C	= carbon
CN	= cyanide radical
con	= control
ep	= endpoint
$F$	= furnace
GK	= gas kinetic model
in	= input
LBL	= laminar boundary-layer model
max	= maximum
min	= minimum
N	= atomic nitrogen
NO	= nitric oxide
NN	= nitrogen-nitrogen (three-body recombination)
N <sub>2</sub>	= molecular nitrogen
$s$	= sample location
( $s$ )	= solid
tot	= total
$w$	= wall
0	= initial
1, 2	= titration or pressure ports

## I. Introduction

A CARBON-BASED ablative thermal protection system (TPS) is often the best choice for mitigating the extreme heat fluxes associated with very-high-speed atmospheric entries [1]. As resins in the carbonaceous ablator pyrolyze during aeroconvective heating, the outer surface becomes almost pure carbon. The ablation process is typically modeled assuming that the ablating surface and ambient

Presented as Paper 2009-4251 at the 41st AIAA Thermophysics Conference, San Antonio, TX, 22–25 June 2009; received 18 August 2010; revision received 13 April 2011; accepted for publication 1 May 2011. Copyright © 2011 by the American Institute of Aeronautics and Astronautics, Inc. The U.S. Government has a royalty-free license to exercise all rights under the copyright claimed herein for Governmental purposes. All other rights are reserved by the copyright owner. Copies of this paper may be made for personal or internal use, on condition that the copier pay the \$10.00 per-copy fee to the Copyright Clearance Center, Inc., 222 Rosewood Drive, Danvers, MA 01923; include the code and \$10.00 in correspondence with the CCC.

Q1 \*Postgraduate Researcher, Molecular Physics Laboratory, 333 Ravenswood Avenue; luningzhang@gmail.com.

†Research Physicist, Molecular Physics Laboratory, 333 Ravenswood Avenue; dusan.pejakovic@sri.com. Member AIAA.

‡Senior Research Scientist, Molecular Physics Laboratory, 333 Ravenswood Avenue; jochen.marschall@sri.com. Senior Member AIAA (Corresponding Author).

§Graduate Student, Engineering Department, 201 Votey Hall, 33 Colchester Avenue; dougherty.max@gmail.com.

¶Professor, Mechanical Engineering Department, 201 Votey Hall, 33 Colchester Avenue; douglas.fletcher@uvm.edu. Fellow AIAA.

gas are in chemical equilibrium [2,3]. However, the chemical equilibrium assumption does not always hold true and simulations of nonequilibrium gas phase and surface chemistry require the use of finite rate surface chemistry models.

A surface reaction can be characterized by a *reaction efficiency* with a value between 0 and 1, defined as the fraction of reactant-surface collisions that result in the reaction. A reaction efficiency is a function of experimental conditions and may depend in general on temperature, pressure, gas and surface composition, and competing surface reaction mechanisms. In simple ablation models, surface reactions are assumed to be first order in reactant concentration, uncoupled and operating in parallel, with rates specified by temperature-dependent reaction efficiencies extracted from various experiments [4–6]. In more sophisticated surface reaction models that consider competing rate processes (adsorption, desorption, Eley–Rideal and Langmuir–Hinshelwood reactions, sublimation, etc.) at finite sets of active surface sites, reaction efficiencies are products of the cumulative effect of the coupled reaction system. For such surface reaction models, experimental reaction efficiencies serve as benchmark data for the adjustment of model parameters. Examples of finite rate carbon/graphite ablation models can be found in the works of Zhlukov and Abe [7], Havstad and Ferencz [8], Chen and Milos [2,9], and Beerman et al. [10].

Because carbon is a key component in both ablative and non-ablative TPS, it often enters into the boundary layer where it can react with the hot plasma gases. Depending on the material and the trajectory conditions, carbon can enter the boundary layer in either solid or gas phases. Direct evidence of solid carbon entering the boundary layer via the mechanism of spallation from test materials in arc-plasma flows has been reported [11]. One of the most important surface reactions for carbon-based TPS materials is the active nitridation of solid carbon by atomic nitrogen:  $N + C_{(s)} \rightarrow CN$ . This reaction contributes directly to TPS mass loss and injects CN into the boundary layer; it is a particularly important heterogeneous reaction because CN is a strong radiator at high temperatures [12,13]. The term “active nitridation” indicates that only gaseous products are formed in this reaction. The importance of this reaction for hyperbolic Earth entries and the lack of experimental data were commented on in a review paper addressing hyperbolic Earth entries [14].

The efficiency of carbon active nitridation by N atoms was first investigated quantitatively by Goldstein in 1964 [15]. Goldstein exposed resistively heated TSX and AGOT graphite samples to microwave-discharged nitrogen at a pressure of 260 Pa and collected condensable products ( $C_2N_2$ , HCN, and  $CO_2$ ) in liquid nitrogen cold traps. The presence of HCN and  $CO_2$  products was attributed to the reactions of carbon with oxygen, water, and hydrogen impurities in the nitrogen flow.  $C_2N_2$  was not detected when only molecular nitrogen was present in the flow, indicating that this species was a result of a carbon nitridation by N atoms, presumably with CN being the initial product. Goldstein obtained the  $C_2N_2/2N$  molar ratios from the chemical analysis of the collected condensable products and estimates of the N-atom flow rate through his discharge system. For TSX graphite, these ratios ranged from  $0.41 \times 10^{-3}$  to  $1.7 \times 10^{-3}$  for temperatures of 1694–2365 K; for AGOT graphite these ratios ranged from  $0.45 \times 10^{-3}$  to  $0.69 \times 10^{-3}$  for temperatures of 2031–2237 K. Although it is difficult to assess the uncertainties of the reaction efficiencies derived from Goldstein’s experiments, this study suggests that only about one in 1000 nitrogen atoms impinging on the surface reacts with carbon.

More recently, Park and Bogdanoff [16] reported a high reaction efficiency of 0.3 for N-atom nitridation of solid carbon at both 300 and 1100 K. Their experiment employed a shock tube to produce a stream of highly dissociated nitrogen, which flowed over a tungsten wire grid coated with lampblack. The lampblack was “graphitized” by heating the grid to  $\sim 1100$  K for 5 s in vacuum. The CN concentration was determined by measuring and modeling (using NEQAIR [17]) the intensity of CN radiation at 386 nm, and the N-atom concentration was calculated by integrating conservation equations. The procedure for obtaining the reaction efficiency in this study was heavily dependent on reactive-flow and radiation modeling.

Subsequently, Suzuki et al. [18,19] studied the ablation of isotropic graphite (Fine Carbon G530, Tokai Carbon Company, Ltd.) in pure nitrogen flows using 110 kW inductively coupled plasma (ICP) wind tunnel. Graphite test samples were in the form of flat-faced cylinders of 3 mm diameter. Tests were conducted at a mass flow of  $2 \text{ g s}^{-1}$ , a pressure of 10 kPa and three different enthalpy levels of 15, 18, and  $20 \text{ MJ kg}^{-1}$ . The N-atom concentration at the stagnation point of the test specimens was computed for each test case using a thermochemical nonequilibrium computational fluid dynamics code [6]. From the computed N-atom densities and the measured sample mass losses, Suzuki et al. [18] reported reaction efficiencies of about  $2.5 \times 10^{-3}$  to  $3.2 \times 10^{-3}$  over a temperature range of 1822–2184 K. More recent measurements by Suzuki et al. [20] have extended the data to lower temperatures where they find a reaction efficiency of about  $1.4 \times 10^{-3}$  at 1400 K. Suzuki et al. [21] have also performed further numerical modeling of their experiments and reported the best agreement between computed and measured carbon ablation when the nitridation efficiency is set to  $3.2 \times 10^{-3}$ . The reaction efficiencies determined by Suzuki et al. [18–21] are similar to those of Goldstein [15] and are about 2 orders of magnitude lower than those obtained by Park and Bogdanoff [16] at lower temperatures.

New laboratory measurements of the active nitridation of solid graphite by N atoms are reported. The experiments were performed using a furnace-heated quartz flow tube coupled to a microwave discharge system. A chemical titration technique was used to determine N-atom concentrations before and after the furnace, thus rigorously bounding the N-atom concentration at the reacting graphite specimen. Carbon mass loss in N/ $N_2$  mixtures was measured over a range of test times, pressures (133–667 Pa), flow speeds ( $16$ – $42 \text{ m s}^{-1}$ ) and temperatures (873–1373 K). Additional experiments, substituting similar concentrations of atomic oxygen and  $O_2$  for atomic nitrogen, were performed to enable a direct comparison of reaction efficiencies for these three reactants in the same experimental setup.

Numerical values for the reaction efficiency were then derived using two simple models of the gas–surface interaction in our flow environment. Any numerical evaluation of reaction efficiency from the experimental data is closely tied to assumptions about the flow environment, the surface reaction mechanism involved, and the values of the transport properties used in the analysis (a statement equally true for all previous published values of reaction efficiency). Therefore, we emphasize the experimental measurements and associated uncertainties and present them in detail so that other researchers can reanalyze our experiments with flow and chemistry models of their own choosing. Finally, our findings are discussed and compared with previously published data.

## II. Experiment

### A. Materials

High-purity graphite (grade DFP-2) was obtained from POCO Graphite in the form of 3.175 mm diameter rods. DFP-2 is a highly purified graphite with a specified impurity content of 5 ppm or less. The material has a density of  $1.77 \text{ g cm}^{-3}$  with a typical particle size of  $4 \mu\text{m}$  and is highly isotropic with respect to its structure and properties. Test samples of the desired length ( $\sim 40$  mm) were cut from longer rods using a razor blade.

The gases used during testing were nitrogen (ultrahigh purity, 99.999%), argon (ultrahigh purity, 99.999%), oxygen (research purity, 99.9999%), and nitric oxide (ultrahigh purity, 99.5%). All gases were obtained from Matheson Tri-Gas and used as received.

### B. Experimental Setup

A diagram of the experimental facility is shown in Fig. 1. A quartz flow tube (22 mm inner diameter) extends through a high-temperature tube furnace with a hot region of approximately 45.5 cm. Atomic nitrogen was generated by flowing  $N_2$  through a microwave discharge located upstream of the furnace. Molecular nitrogen was introduced upstream of the discharge through a flow controller and

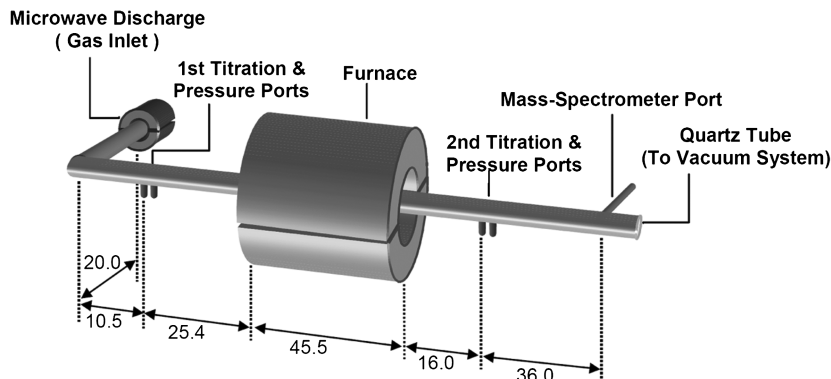


Fig. 1 Diagram of the experimental facility; dimensions are given in centimeters.

evacuated downstream of the furnace by a dry scroll pump. The power delivered to the microwave discharge was typically 90–95 W. Because the discharge was operated at constant power under steady-state temperature and gas flow conditions, the  $N_2$  dissociation fraction remained essentially constant during any given experimental run. Gas pressures were measured before and after the furnace using a capacitance manometer. The temperatures of the flow tube were measured using “stick-on” type  $K$  thermocouples at the location of both pressure ports and near the entrance and exit of the furnace. The gas pressure and bulk velocity in the flow tube were varied by simultaneous adjustment of the incoming  $N_2$  flow rate and a throttling valve in the downstream pumping manifold.

The flows of  $N$  atoms entering and exiting the furnace were quantified by gas-phase titration with nitric oxide via the gas-phase reaction  $N + NO \rightarrow N_2 + O$ . This reaction produces one oxygen atom for every  $NO$  consumed and is very rapid, with a room-temperature rate coefficient of  $3 \times 10^{-11} \text{ cm}^3 \text{ molecule}^{-1} \text{ s}^{-1}$  [22]. At the titration endpoint, all  $N$  atoms are consumed and the number density of added  $NO$  is equal to the number density of  $N$  atoms entering the titration region. The  $N$ -atom mole fractions at the titration ports were then calculated from the measured  $N_2$  and  $NO$  mass flows using the formula

$$\chi_N = \frac{\dot{m}_{NO,ep}/M_{NO}}{\dot{m}_{N_2,in}/M_{N_2} + 0.5\dot{m}_{NO,ep}/M_{NO}} \quad (1)$$

where  $\dot{m}_{N_2,in}$  is the mass flow rate of  $N_2$  introduced upstream of the discharge,  $\dot{m}_{NO,ep}$  is the mass flow rate of  $NO$  at the endpoint, and  $M_{NO}$  and  $M_{N_2}$  are molar masses. Under our experimental conditions the  $N$ -atom mole fractions were always less than 1%. The local  $N$ -atom concentrations follow from the ideal gas law and the pressures and tube wall temperatures (assumed equal to the gas temperatures) measured at the titration locations.

Titration endpoints were determined redundantly, by the mass spectroscopic detection of  $NO$  in the gas phase and by optical spectroscopic detection of  $NO_2$  chemiluminescence above the endpoint. Nitrogen dioxide chemiluminescence results from the reaction of excess  $NO$  with titration-produced  $O$  atoms beyond the endpoint [23]. Mass spectroscopy was performed by sampling the gas flow downstream of both titration ports through a leak valve into turbo-pumped chamber equipped with a residual gas analyzer (Stanford Research Systems RGA300). Optical emission spectroscopy was performed by collecting fluorescence downstream of the titration ports using an optical fiber probe connected to an optical spectrometer (Newport model OSM-100-UV-NIR).

An example of a titration endpoint determination by these two techniques is shown in Fig. 2. Given that the endpoint is not sharp, the flow rate of  $NO$  at the endpoint has an estimated experimental uncertainty of about  $\pm 5\%$  upstream of the furnace and about  $\pm 15\%$  downstream of the furnace where  $N$ -atom concentrations are lower. Similar uncertainties are translated into mole fractions calculated by Eq. (1).

### C. Experimental Procedures

Carbon samples were mounted in a quartz fixture that aligned the axis of the sample with the centerline of the flow tube (see Fig. 3.) The sample length protruding out of the holder was typically three-fourths of the total sample length or about 30 mm. Mounted samples were positioned near the midpoint of the furnace, with the front face of the samples about 22 cm from the upstream entrance of the furnace.

Samples were heated at a rate of  $5\text{--}10 \text{ K min}^{-1}$  to the target test temperature under a low-pressure flow of  $N_2$ . When the target temperature was reached, gas flows and pressures were adjusted to the desired levels and the discharge was activated for a prescribed time interval. After this test time, the discharge was turned off and the furnace cooled at a similar rate under continuing gas flow until the temperature dropped below  $\sim 473 \text{ K}$ . Each sample was weighed immediately before it was placed into the flow tube and immediately after it was removed from the flow tube, using an analytic balance (Mettler Toledo XP105) with a 0.01 mg resolution.

Nitric oxide titration measurements were performed for each unique flow condition with the sample holder in place but no sample

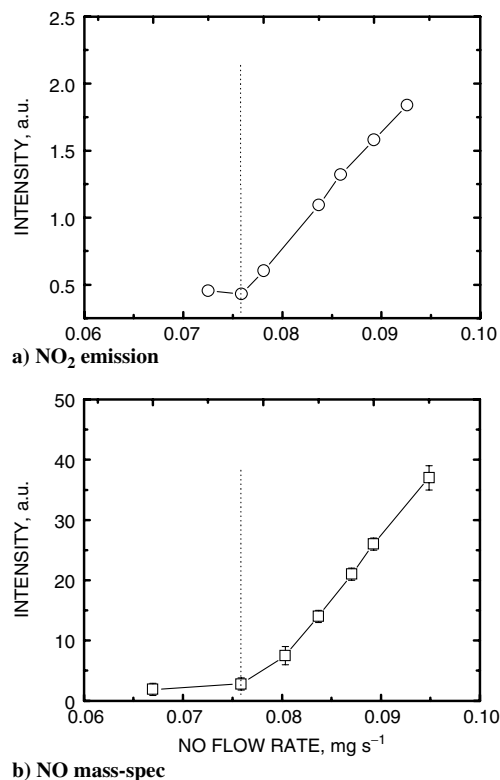


Fig. 2 Detection of the  $N + NO \rightarrow N_2 + O$  titration endpoint by the a) rise of  $NO_2$  emission intensity and b) detection of  $NO$  in the gas phase.

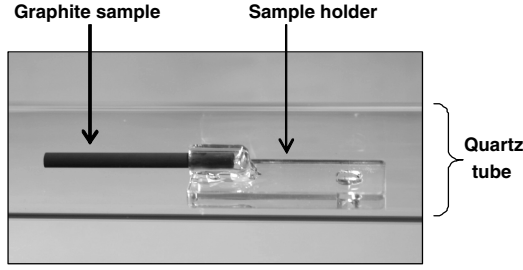


Fig. 3 Cylindrical graphite specimen mounted in quartz sample holder positioned inside the quartz flow tube.

present. This was done to capture the pressure drop caused by the sample holder while avoiding potential complications due to the gas-phase reaction of N atoms with CN produced by carbon nitridation.

Control experiments were performed at several test conditions, in nitrogen flows without discharge activation and in pure argon flows. Some mass loss was observed in all cases, perhaps indicating the volatilization of some hydrocarbons from the graphite samples or the presence of a residual oxygen source (leak) in the flow system. This background mass loss, which typically ranged from 5 to 10% of that measured when the discharge was activated, was subtracted from sample mass losses used to evaluate the efficiency of the  $N + C_{(s)} \rightarrow CN$  reaction.

### III. Data Analysis

#### A. Reactive-Flow Model

The N-atom concentration at the sample location is required to evaluate the efficiency of the carbon nitridation reaction. Because gas-phase and surface recombination reactions consume N atoms as they flow through the system, the N-atom mole fraction downstream of the furnace is always less than that upstream of the furnace. The *absolute* upper and lower limits on the N-atom concentration at the location of the graphite test specimen can be calculated as

$$C_{N,\max} = \frac{[\chi_N P]_1}{RT_F} \quad ()$$

and

$$C_{N,\min} = \frac{[\chi_N P]_2}{RT_F} \quad ()$$

We have used a simple reactive-flow model in axisymmetric geometry to obtain an improved estimate of the N-atom concentration at the sample location by interpolation. The flow model assumes that the bulk gas flow is laminar and suitably described by the Hagen–Poiseuille flow relation incorporating the ideal gas law:

$$P \frac{dP}{dz} = - \frac{128 \dot{m}_{N_2} \mu_{N_2} RT}{\pi d^4 M_{N_2}} \quad (3)$$

Because of the low  $N_2$  dissociation fraction in our system, we assume that the flow behavior is dominated by the transport properties of molecular nitrogen and is unaffected by compositional variations as N atoms recombine. All variables on the right-hand side of Eq. (3) are measured or known. Because the tube length between the two titration ports contains sections both inside and outside of the furnace, the temperature and viscosity vary with axial position. The variation of tube wall temperature with axial position was approximated by linear and cubic functions interpolating between measured wall and furnace temperatures. The temperature dependence of nitrogen viscosity was taken from Touloukian et al. [24] The additional pressure drop associated with sample and sample holder inside the tube was modeled as a constriction of the tube diameter over a short section at the sample location.

Equation (3) was integrated numerically from  $z = 0$  to  $L$ , using the boundary condition  $P(0) = P_1$ . The bulk flow velocity was then calculated from  $P(z)$  as

$$v(z) = \frac{4 \dot{m}_{N_2} RT}{\pi d^2 M_{N_2} P(z)} \quad (4)$$

Wall losses for the  $N + N$  surface reaction are specified by the recombination efficiency  $\gamma_N$ , defined as the fraction of N-atom collisions with the tube wall that result in removal of an N atom from the gas phase. Published values of  $\gamma_N$  on quartz range widely, from  $10^{-6}$  to  $10^{-3}$ , generally increasing slightly with temperature over the temperature range of our experiments [25–28]. Gas-phase N-atom losses by the three-body reaction  $N + N + N_2 \rightarrow 2N_2$  are specified by the temperature-dependent rate constant  $k_{NN} = 300 \exp(500/T) \text{ m}^6 \text{ mol}^{-2} \text{ s}^{-1}$ , recommended by Baulch et al. [29] The variation of N-atom concentration with axial location was modeled by the differential equation

$$\frac{dU}{dz} = -U \frac{\gamma_N \bar{v}_N}{vd} - U^2 \frac{2k_{NN} C_{N_2}}{v^2} \quad (5)$$

where the axial flux of N atoms  $U(z)$  is equal to the product  $v(z)C_N(z)$ . Equation (5) is derived by equating the difference in the net N-atom flows (mol/s) into and out of a disk of differential thickness  $\delta z$  to the N-atom losses (mol/s) by recombination on the tube walls (first term on the right-hand side) and in the gas phase (second term on the right-hand side). This formulation assumes that the flow approaching the test specimen is laminar and that the diffusion of N atoms to the walls is effectively instantaneous, and therefore there are no radial concentration gradients. The quality of these assumptions is confirmed in the Experimental Results section, by computing the Reynolds number and the tube surface Damköhler number (the ratio of the characteristic radial diffusion time  $d^2/4D$  to the characteristic surface reaction time  $d/\gamma_N \bar{v}$ ) for the range of experimental conditions in this study. Equation (5) was integrated numerically from  $z = 0$  to  $L$ , using the boundary condition  $U(0) = v(0)C_N(0)$ , and the N-atom concentration was calculated from the solution  $U(z)$  as  $C_N(z) = U(z)/v(z)$ .

The interpolation procedure to derive the N-atom concentration at the sample location was performed as follows. First, the effective constricted tube diameter used to model the pressure drop at the sample location was adjusted until the solution of Eq. (3) reproduced the measured value of  $P_2$ . Then, the value of the wall recombination efficiency  $\gamma_N$  at the furnace temperature was adjusted until the solution of Eq. (5) reproduced the concentration  $C_{N,2}$  calculated from the measured N-atom mole fraction. The room-temperature value of  $\gamma_N$ , used for the portion of tube outside the furnace, was set to be  $3 \times 10^{-5}$ . Over our entire range of experimental conditions, values of the effective tube diameter ranged from about 13 to 15 mm, and values of  $\gamma_N$  at the furnace temperature ranged from about 2 to  $7 \times 10^{-4}$ . These parameter adjustments are deemed consistent with our use of this simple reactive-flow model as an interpolation tool for estimating  $C_N$  at the sample location.

#### B. Computation of the Reaction Efficiency

The reaction efficiency  $\gamma_{CN}$  was computed from the measured carbon mass loss, the interpolated N-atom concentration at the sample location, the test time, and the sample dimensions. For this analysis it was assumed that all measured mass loss occurred on the length of test specimen protruding from the quartz sample holder,  $L_s$ , and that samples experienced negligible dimensional changes during the tests. For our test conditions the latter assumption is certainly true on a macroscopic scale, although some roughening of the surface during active nitridation was observed, leading, on a microscopic scale, to increased surface area available for reaction. We did observe some color changes on sample surfaces within the quartz holder, indicating some surface reaction on this portion of the test specimens as well. However, visual inspection of the sample surface after testing indicates that carbon nitridation is much less effective within the holder than on the extended sample. We confirmed this by testing a short sample that did not protrude from the holder and found that the mass loss rate from the sample surface within the holder is about 35 times smaller than from the protruding sample surface. Thus the

possible error of our estimate of  $\gamma_{\text{CN}}$  introduced by our assumption that all carbon is lost from the protruding sample length is only on the order of 1%.

Two simple models of gas–surface interactions were used to evaluate  $\gamma_{\text{CN}}$ : a gas-kinetic (GK) model and a simple laminar boundary-layer (LBL) model. Both models presume that the  $\text{N} + \text{C}_{(s)} \rightarrow \text{CN}$  reaction is first order in N-atom concentration and independent of pressure and that it proceeds by the direct reaction of an impinging nitrogen atom with a carbon atom in the surface to form a CN molecule that instantly desorbs; no reactant adsorption steps or intermediate surface species are considered. The primary difference between these two models is that the LBL model attempts to capture reactant and product transport limitations on the rate of surface reaction, whereas the GK model implicitly assumes that transport limitations are negligible.

The LBL and GK models can be derived from the same basic starting point. The reaction flux ( $\text{mol m}^{-2} \text{s}^{-1}$ ) as a function of axial location on the cylindrical sample surface under steady-state, isothermal conditions can be written as

$$R(x) = k_f C_{\text{N},w}(x) - k_b C_{\text{CN},w}(x) \quad (6)$$

where  $x$  defines the axial position ( $x = 0$  to  $L_s$ ) and the subscript  $w$  indicates the local N and CN concentrations at the sample surface. The forward reaction-rate constant is specified as the reaction efficiency times the N-atom impingement flux:

$$k_f = \gamma_{\text{CN}} \frac{\bar{v}_{\text{N}}}{4} \quad (7)$$

and the backward rate constant is determined by the thermodynamic relationship

$$k_b = \frac{k_f}{K_{\text{eq}}(T)} \quad (8)$$

The local carbon mass loss flux ( $\text{kg m}^{-2} \text{s}^{-1}$ ) can then be expressed as

$$\dot{m}_c(x) = M_C \frac{\gamma_{\text{CN}} \bar{v}_{\text{N}}}{4} \left[ C_{\text{N},w}(x) - \frac{1}{K_{\text{eq}}(T)} C_{\text{CN},w}(x) \right] \quad (9)$$

and the net mass loss from a carbon test specimen is given by

$$\Delta m_C = \pi d_s \Delta t M_C \frac{\gamma_{\text{CN}} \bar{v}_{\text{N}}}{4} \int_0^{L_s} \left[ C_{\text{N},w}(x) - \frac{1}{K_{\text{eq}}(T)} C_{\text{CN},w}(x) \right] dx \quad (10)$$

In Eq. (10) we have made the assumption that carbon loss from the sample face is minimal compared with carbon loss from the cylindrical surface (typical surface area ratio of 1:40).

The evaluation of Eq. (10) requires functional forms for the wall concentrations of N and CN along the cylindrical sample surface. In the LBL model, we make the approximation that they can be adequately represented using the analytic series solutions for first-order reversible surface reactions in a laminar boundary-layer flow as presented by Acrivos and Chambré [30] for a flat-plate geometry. These solutions are

$$C_{\text{N},w}(x) = C_{\text{N}} \left[ 1 + \frac{\sum_{m=1}^{\infty} \alpha_m y^m}{1 + \frac{k_b D_{\text{N}} S C_{\text{N}}^{1/3}}{k_f D_{\text{CN}} S C_{\text{CN}}^{1/3}}} \right] \quad (11)$$

and

$$C_{\text{CN},w}(x) = \frac{D_{\text{N}} S C_{\text{N}}^{1/3}}{D_{\text{CN}} S C_{\text{CN}}^{1/3}} [C_{\text{N}} - C_{\text{N}}(x)] \quad (12)$$

with

$$y \equiv \left[ \frac{k_f + k_b \frac{D_{\text{N}} S C_{\text{N}}^{1/3}}{D_{\text{CN}} S C_{\text{CN}}^{1/3}}}{0.339 D_{\text{N}} S C_{\text{N}}^{1/3}} \right] \sqrt{\frac{x \mu}{\rho v_s}} \quad (13)$$

In Eqs. (11) and (12),  $C_{\text{N}}$  is taken as the N-atom concentration at the sample location predicted by the reactive-flow model described in the previous section. The coefficients  $\alpha_m$  are given by the recurrence formula

$$\alpha_m = -\alpha_{m-1} \frac{\Gamma(\frac{2+2m}{3})}{\Gamma(\frac{2}{3}) \Gamma(\frac{3+2m}{3})} \quad (14)$$

with  $\alpha_0 = 1$ .

Numerical evaluation of Eqs. (11–13) requires temperature-dependent effective mixture diffusion coefficients and gas viscosities. Because N and CN are very dilute, their effective multispecies diffusion coefficients are set equal to their binary diffusion coefficients in  $\text{N}_2$ . We used the collision integrals of Wright et al. [31,32] to compute the binary diffusion coefficients from the well-known Chapman–Enskog equation. The bulk properties of molecular nitrogen were used to compute the gas density and viscosity in the Schmidt numbers and in the square-root term of Eq. (13). The temperature-dependent equilibrium constant for the  $\text{N} + \text{C}_{(s)} \rightarrow \text{CN}$  reaction was taken from the HSC Chemistry software database [33].

The GK model is obtained from Eq. (10) by making two further simplifications: ignoring the backward reaction and setting  $C_{\text{N},w}(x)$  equal to the constant value predicted by our reactive-flow model. The first simplification rests on the fact that  $C_{\text{CN},w}$  is always less than  $C_{\text{N},w}$  and that  $K_{\text{eq}}(T)$  is very large for all our experimental temperatures [33]. The second simplification presumes that pressures are low enough, temperatures and gas velocities are high enough, and the surface reaction is slow enough, such that transport limitations through a concentration boundary layer around the sample are negligible. This set of assumptions leads to a simple analytic expression:

$$\gamma_{\text{CN,GK}} = \frac{4 \Delta m_C}{C_{\text{N}} M_C \Delta t \pi d_s L_s \bar{v}_{\text{N}}} \quad (15)$$

Equation (15) allows the direct calculation of the reaction efficiency in the GK model. For the LBL model, the best value of  $\gamma_{\text{CN,LBL}}$  for a particular test run is determined by iteratively adjusting its value to minimize the difference between the computed and experimental mass loss. Insertion of  $C_{\text{N}} = C_{\text{N,max}}$  into Eqs. (11) and (12) will give a lower limit on  $\gamma_{\text{CN}}$ , and the use of  $C_{\text{N}} = C_{\text{N,min}}$  an upper limit, for the LBL model. Similarly, the insertion of these values into Eq. (15) gives the lower and upper limits in the GK model.

### C. Flow Separation Modeling

Because flow separation and recirculation could conceivably influence local mass loss rates by enhancing the transport of reactants and products near the graphite surface, the flow separation caused by different tip shapes and the sample/holder junction was investigated numerically using commercially available FLUENT computational fluid dynamics (CFD) software. The nitrogen flow down the tube and around the specimen was modeled as steady-state, two-dimensional, and axisymmetric. An implicit, finite volume, pressure-based solver was used to model the flow, and this solver included the Spalart–Allmaras turbulence model. The Reynolds number for these flows based on sample length ranged from  $\sim 30$  to 50, clearly indicating laminar flow conditions. However, initial computational simulations resulted in nonphysical results (including negative pressures) and so subsequent computations were done with the aforementioned turbulence model included, and these produced physical results that were clearly laminar flow solutions without any evidence of unsteadiness. As all cases were run with the same code configuration, we believe that the trends are reliable. Four equations were solved in order to obtain a solution: continuity (conservation of mass), momentum (considered for axial and radial directions), and the transport equation for the turbulent kinematic viscosity. Pressure was discretized using the PRESTO! (pressure staggering option) scheme. Both momentum and turbulent viscosity were computed with

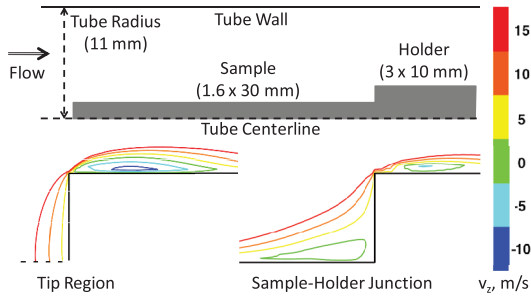


**Fig. 4** Computational geometry (top) and contours of axial velocity component near the tip (lower left) and sample-holder junction (lower right) computed at  $T = 1273$  K,  $P_s = 148$  Pa, and  $v_s = 28$  ms $^{-1}$ . Negative values of axial velocity indicate recirculation regions.

second order upwinding schemes. Pressure-velocity coupling was performed using the SIMPLE (semi-implicit method for pressure-linked equations) scheme.

The graphite specimen and sample holder were modeled as adjoining cylinders, with radius and length of 1.6 and 30 mm, and 3.0 and 10 mm, respectively (see Fig. 4). In the computational domain the sample was placed 480 mm downstream of the inlet to allow the flow to become fully developed before reaching the sample. An additional 100 mm were modeled downstream of the sample. The domain was discretized with a grid consisting of about 200,000 nodes (for the final cases). Grid convergence was considered adequate after the residuals had dropped by at least 5 orders of magnitude and leveled off.

Three tip geometries (flat-faced, conical, and hemispherical) were modeled at 1273 K for two different velocity and pressure test conditions (16 ms $^{-1}$  and 376 Pa; 28 ms $^{-1}$  and 148 Pa). All cases showed a recirculation region at the junction of the sample and the sample holder. The flat-faced sample also showed a second region of recirculation immediately downstream of the tip (see Fig. 4). Computational results from this CFD modeling are discussed in the context of our experiments in Sec. IV.A.

## IV. Experimental Results

### A. Experiments at 1273 K

Experimental conditions and measurement results for 28 different nitridation tests conducted at a furnace temperature of 1273 K in two different quartz flow tubes are listed in Tables 1 and 2. The first columns of Tables 1 and 2 list identification codes for each individual test, where the leading capital letter corresponds to a unique combination of flow velocity and pressure, the following number indicates the flow tube used (either 1 or 2), and the final number identifies a specific graphite sample. Lowercase letters appended to the final number indicate repeated tests run on the same sample.

Measurement errors in the pressures at the titration ports and the nitrogen flow rates are no more than 1%. The pressures and bulk velocities at the sample computed from Eqs. (3) and (4) must have somewhat higher uncertainties, but they are still not likely to exceed 5%. The mole fractions at the titration ports have uncertainties on the order of 5% at port 1 and 15% at port 2 associated with identifying the exact titration endpoint. The estimated uncertainty in the N-atom concentration at the sample obtained from the reactive-flow model interpolation procedure is  $\sim 20\%$ . For comparison, the maximum and minimum concentration bounds give values 30 to 110% higher and 15 to 50% lower, respectively, than the value derived using reactive-flow model.

For the conditions listed in Table 1, tube Reynolds numbers at the sample location range from about 3 to 22 and the entrance lengths for fully developed laminar flow are always less than 3 cm. Thus, the gas flow approaching the test specimens should be laminar. The tube surface Damköhler numbers based on a conservative (high) value for the N-atom surface recombination efficiency on quartz of  $10^{-3}$  are all less than 0.12, indicating that diffusion is faster than the rate of atom loss on the tube walls and implying a relatively uniform N-atom concentration (i.e., independent of radial coordinate) approaching the test specimen. A less conservative (lower) value for N-atom loss efficiency would further decrease the estimated Damköhler numbers.

Table 2 lists the corresponding test times, the initial sample mass, the total carbon mass loss, the control (background) mass loss, and the sample length extending from the quartz sample holder, along with the maximum, best, and minimum values of the reaction

**Table 1** Flow conditions for experiments conducted at 1273 K

Test ID	$\dot{m}_{N_2, \text{in}}$ mg s $^{-1}$	$P_1$ Pa	$P_2$ Pa	$P_s$ Pa	$v_s$ ms $^{-1}$	$\chi_{N,1}$ %	$\chi_{N,2}$ %	$C_N, 10^{-4}$ mol m $^{-3}$		
								Max	Best	Min
A-1-13a	2.5	166.7	135.1	155.2	16.0	0.216	0.133	0.314	0.236	0.199
A-1-13b	2.5	166.7	135.1	155.2	16.0	0.216	0.133	0.314	0.236	0.199
B-1-13c	4.1	263.3	228.9	251.6	16.1	0.435	0.174	1.034	0.634	0.418
C-1-15	6.0	387.2	350.8	375.6	16.0	0.526	0.179	1.867	1.030	0.634
D-1-18	8.4	533.3	496.5	521.6	16.1	0.588	0.155	2.899	1.400	0.766
E-1-12	10.4	600.6	559.3	587.7	17.6	0.568	0.164	3.156	1.590	0.910
F-1-17	10.6	666.6	628.2	654.7	16.1	0.563	0.163	3.484	1.760	1.006
G-1-11a	4.2	166.7	109.7	147.2	28.1	0.270	0.140	0.375	0.249	0.195
G-1-11b	4.2	166.7	109.7	147.2	28.1	0.270	0.140	0.375	0.249	0.195
H-1-14a	6.9	263.3	201.6	243.4	28.0	0.378	0.191	0.870	0.578	0.439
H-1-14b	6.9	263.3	201.6	243.4	28.0	0.378	0.191	0.870	0.578	0.439
I-1-19	10.4	386.6	320.0	366.2	28.3	0.459	0.212	1.588	1.020	0.733
J-1-21	14.6	533.3	465.3	512.8	28.2	0.453	0.197	2.196	1.370	0.954
K-1-23	16.5	600.0	531.4	579.6	28.2	0.427	0.188	2.338	1.470	1.032
L-1-22	18.3	666.6	598.1	645.9	28.2	0.399	0.185	2.433	1.580	1.130
C-2-38	6.0	386.6	352.0	375.6	16.0	0.421	0.143	1.494	0.824	0.507
C-2-42	6.0	386.6	352.0	375.6	16.0	0.421	0.143	1.494	0.824	0.507
M-2-34	8.1	386.6	338.6	370.8	21.7	0.411	0.115	1.442	0.718	0.405
M-2-37	8.1	386.6	338.6	370.8	21.7	0.411	0.115	1.442	0.718	0.405
I-2-36	10.4	386.6	324.0	366.2	28.2	0.352	0.128	1.227	0.703	0.445
N-2-39	15.0	386.6	291.2	356.8	41.8	0.277	0.111	0.940	0.614	0.376
N-2-35	15.0	388.0	293.3	356.8	41.8	0.277	0.111	0.940	0.614	0.376
I-2-54	10.4	386.6	322.1	366.2	28.3	0.352	0.128	1.227	0.703	0.445
G-2-61a	4.2	166.7	107.1	148.0	28.0	0.184	0.100	0.257	0.173	0.140
G-2-61b	4.2	166.7	107.1	148.0	28.0	0.184	0.100	0.257	0.173	0.140
G-2-62a	4.2	166.7	107.1	148.0	28.0	0.184	0.100	0.257	0.173	0.140
G-2-62b	4.2	166.7	107.1	148.0	28.0	0.184	0.100	0.257	0.173	0.140
K-2-63	16.5	600.0	530.6	580.2	28.2	0.404	0.114	2.216	1.220	0.624

**Table 2** Mass loss data and computed reaction efficiencies at 1273 K for the flow conditions listed in Table 1

Test ID	$\Delta t$ min	$m_0$ mg	$\Delta m_{C,tot}$ mg	$\Delta m_{C,con}$ mg	$L_s$ mm	$\gamma_{CN,GK}, 10^{-3}$			$\gamma_{CN,LBL}, 10^{-3}$		
						Max	Best	Min	Max	Best	Min
A-1-13a	120	515.70	0.76	0.08	28.5	3.68	3.29	2.33	4.60	3.88	2.91
A-1-13b	150	514.92	0.73	0.10	28.0	2.72	2.48	1.73	3.34	2.82	2.12
B-1-13c	145	514.19	1.26	0.15	28.0	2.57	1.68	1.04	2.86	1.89	1.16
C-1-15	144	530.75	2.96	0.23	29.0	4.15	2.48	1.41	4.87	3.00	1.66
D-1-18	155	535.82	4.08	0.35	29.5	4.38	2.28	1.16	5.12	2.80	1.35
E-1-12	125	547.31	3.45	0.33	30.5	3.74	2.01	1.08	4.25	2.43	1.22
F-1-17	133	560.58	3.70	0.39	30.5	3.41	1.81	1.00	3.83	2.19	1.10
G-1-11a	125	528.68	1.27	0.08	28.5	6.44	5.24	3.35	8.10	6.33	4.20
G-1-11b	120	527.42	1.00	0.07	28.5	5.16	4.26	2.68	6.37	4.99	3.31
H-1-14a	123	524.06	1.86	0.13	28.5	4.41	3.34	2.23	5.15	3.90	2.60
H-1-14b	152	522.20	2.32	0.16	28.5	4.45	3.37	2.25	5.20	3.95	2.63
I-1-19	146	535.66	3.94	0.23	29.0	4.78	3.36	2.20	5.65	4.06	2.61
J-1-21	156	523.98	5.96	0.07	28.5	5.43	3.78	2.36	6.97	4.85	3.03
K-1-23	146	535.08	4.81	0.08	28.5	4.32	3.02	1.91	5.33	3.74	2.35
L-1-22	146	537.21	4.65	0.08	28.5	3.82	2.72	1.77	4.65	3.33	2.16
C-2-38	153	558.39	1.07	0.06	31.0	1.63	1.01	0.55	1.80	1.11	0.61
C-2-42	161	558.45	1.26	0.06	29.7	1.92	1.19	0.65	2.15	1.32	0.73
M-2-34	151	546.68	1.32	0.05	30.0	2.68	1.53	0.75	3.02	1.71	0.85
M-2-37	160	563.82	1.24	0.06	31.5	2.24	1.28	0.63	2.50	1.41	0.70
I-2-36	180	545.21	1.58	0.06	30.0	2.45	1.57	0.89	2.74	1.73	0.99
N-2-39	143	555.08	1.11	0.05	30.3	2.52	1.56	1.01	2.80	1.70	1.12
N-2-35	172	559.36	1.36	0.06	30.2	2.58	1.59	1.03	2.85	1.74	1.14
I-2-54	174	581.53	2.15	0.06	31.2	3.36	2.14	1.22	3.86	2.44	1.40
G-2-61a	170	550.65	0.90	0.02	29.5	4.63	3.96	2.52	5.67	4.60	3.10
G-2-61b	148	549.75	0.76	0.02	29.5	4.48	3.83	2.44	5.47	4.43	2.98
G-2-62a	86	472.74	0.49	0.01	24.5	6.08	5.12	3.31	7.56	6.12	4.12
G-2-62b	288	472.28	1.21	0.03	24.0	4.48	3.83	2.44	5.45	4.41	2.97
K-2-63	136	535.67	2.45	0.07	29.0	3.77	1.93	1.06	4.36	2.23	1.23

coefficients computed with the GK and LBL models. Uncertainties in the measure quantities are  $\pm 1$  min for the test time,  $\pm 0.02$  mg in the mass loss, and  $\pm 1$  mm in the exposed sample length. The estimated uncertainty of the “best” values of  $\gamma_{CN,GK}$  and  $\gamma_{CN,LBL}$  is about 25%. We note that this uncertainty reflects the propagation of experimental errors and does not include any errors associated with the models chosen for deriving reaction efficiencies from the data.

For the GK model, the best reaction efficiencies in Table 2 range from about  $1.0 \times 10^{-3}$  to  $5.2 \times 10^{-3}$ , with an average and standard deviation of  $(2.7 \pm 1.2) \times 10^{-3}$  for the entire set of 28 tests. The reaction efficiencies derived from the LBL analysis are systematically higher than the GK values by 10 to 30%; the average LBL value and standard deviation are  $(3.2 \pm 1.5) \times 10^{-3}$ . The slightly higher LBL values are caused by a slightly lower concentration of N atoms at the sample surface due to diffusion limitations through the laminar boundary layer over the cylindrical sample surface. However, the difference between the GK- and LBL-derived values is not of great practical significance, given that it is less than the standard deviation of the average best GK value. Similar or larger differences are observed between measurements repeated under nominally identical test conditions, for example conditions A-1, G-1, and G-2. Moreover, measurements made under nominally identical pressure and velocity conditions in tube 2 generate reaction efficiencies that are  $\sim 50\%$  or more lower than those in tube 1 (compare, e.g., tests G-1 with G-2, I-1 with I-2, and K-1 with K-2). Tubes 1 and 2 are made of the same grade of quartz and have the same dimensions, so the reason for this difference is not known.

Two implicit assumptions in the analyses outlined in Sec. II are 1) the carbon mass loss at a fixed test condition is linear in time and 2) the net carbon flux leaving the sample under isothermal conditions is a linear function of the local N-atom concentration. These assumptions are tested against experimental data in Figs. 5 and 6, which show that the expected trends are reasonably well followed, although with considerable scatter in the latter case. This scatter suggests considerable variation in the experimental reproducibility and/or additional dependencies of the carbon mass flux on other experimental parameters such as velocity and pressure.

One possibility for a dependence of the carbon mass flux on pressure and velocity is that the reactant and product fluxes through

the laminar boundary layer above the sample are determined by transport limitations, not the surface reaction rate. If the efficiency of the surface reaction is transport-limited and reactant/product transport *is not* considered in the data analysis (as in the GK analysis), values of  $\gamma_{CN}$  are expected to be proportional to velocity and total pressure as  $v_s^\alpha P_s^\beta$ . This dependence arises because the laminar boundary-layer thickness grows in proportion to the local Reynolds number and the diffusion rate through a boundary layer varies inversely with the total pressure [34]. If the surface reaction is transport-limited and reactant/product transport *is* considered in the data analysis (as in the LBL analysis), no such dependence for  $\gamma_{CN}$  is expected. For either type of data analysis, no velocity and pressure dependence for  $\gamma_{CN}$  is expected if the efficiency of the surface reaction is reaction-rate limited.

Separate linear regression analyses of the best GK and LBL reaction efficiencies in Table 2 were performed and yielded

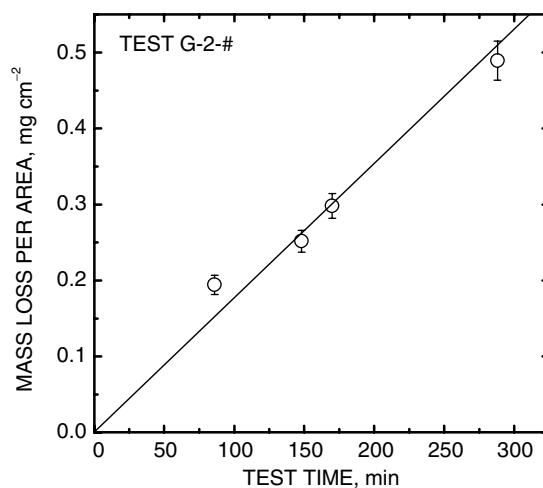


**Fig. 5** Carbon mass loss per surface area as a function of time at 1273 K for test series G-2-(61a, 61b, 62a, and 62b) shown with a linear fit through the origin.

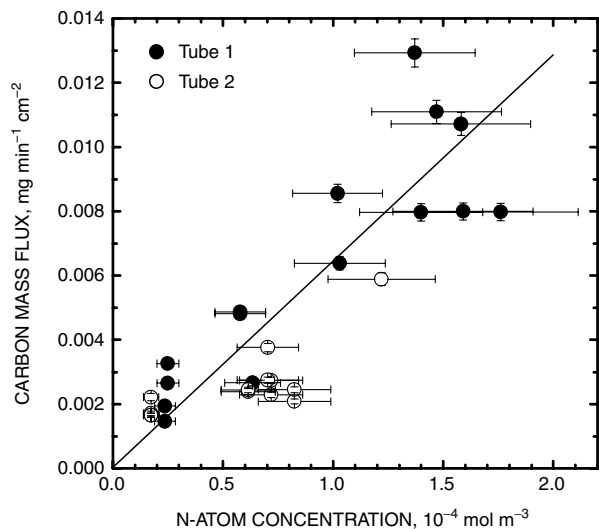


**Fig. 6** Carbon mass flux at 1273 K versus Natom concentration at the sample location, shown with a linear fit through origin.

essentially identical values of  $\alpha = 0.40$  and  $\beta = -0.45$ . The GK and LBL reaction efficiencies are plotted versus  $v_s^{0.40} P_s^{-0.45}$  in Fig. 7. Although scatter remains substantial, Fig. 7 reveals a trend of increasing reaction efficiency with increasing values of  $v_s^{0.40} P_s^{-0.45}$ . The reaction efficiencies increases by a factor of about 2.5 to 3 over the range of  $v_s^{0.40} P_s^{-0.45}$  plotted, for both  $\gamma_{CN,GK}$  and  $\gamma_{CN,LBL}$ .

Thus, we find an apparent dependence of reaction efficiency on the experimental pressure and velocity, but cannot ascribe this dependence to diffusive transport limitations since both the GK and LBL analyses show the same behavior.

To investigate possible enhancement of reactant and product transport at the graphite surface by flow separation effects near the sample tip, additional experiments at 1273 K were conducted at  $v_s^{0.40} P_s^{-0.45} = 0.21$  (velocity of 16  $\text{ms}^{-1}$  and pressure of 376 Pa) and  $v_s^{0.40} P_s^{-0.45} = 0.40$  (velocity of 28  $\text{ms}^{-1}$  and pressure of 148 Pa), using graphite specimens with either a hemispherical cap (1.6 mm radius) or a sharp cone (30° apex angle) facing into the flow. A similar (factor of 2 to 3) increase in reaction efficiency with increasing  $v_s^{0.40} P_s^{-0.45}$  was observed for both of these tip shapes, as was the case for the flat-faced samples. No systematic differences in reaction efficiencies were found for different tip shapes at the same value of  $v_s^{0.40} P_s^{-0.45}$ .

Using the CFD model described in Sec. III.C, the quantity  $v_s^{0.40} P_s^{-0.45}$  was calculated from the bulk velocity and average pressure 10 mm upstream of the sample tip for each of our test specimens and conditions. Recirculation regions were identified

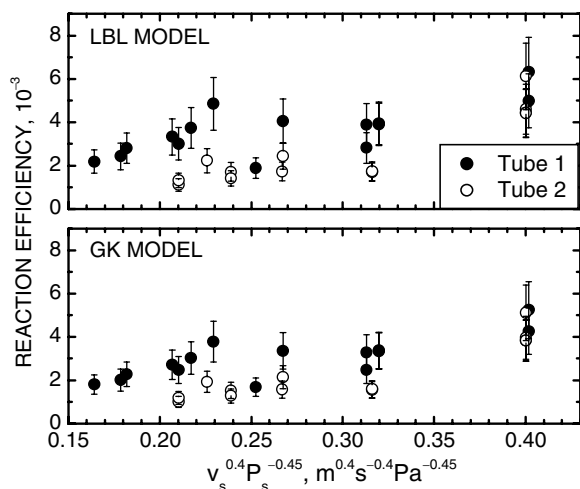


**Fig. 7** Reaction efficiency at 1273 K versus  $v_s^{0.40} P_s^{-0.45}$ .

from vector plots of axial velocities and separation lengths were defined as the distance between the extreme points of recirculation regions on the sample surface. The CFD results predict the total separation length to increase for all sample geometries with increasing  $v_s^{0.40} P_s^{-0.45}$ , which seems to coincide with the observed trend in the reaction efficiencies. However, the calculations also predict that separation lengths for the flat-faced specimens are always as much as 40–60% larger than for the samples with hemispherical or conical tips under the same conditions, whereas no such trend in reaction efficiencies was observed in the experiments. Therefore, we cannot conclude that flow separation and recirculation phenomena are responsible for the  $v_s^{0.40} P_s^{-0.45}$  dependence of the derived values of  $\gamma_{CN}$ , at least within the range of flow velocities and pressures used and with the present scatter in the experimental data.

The reason for the observed  $v_s^{0.40} P_s^{-0.45}$  dependence remains uncertain and we make no corrections in the value of the reaction efficiency due to flow separation effects. We derive the most probable value of  $\gamma_{CN}$  at 1273 K by simply averaging all experimental values in Table 2. We consider the LBL values more reliable than the GK values because they take into account diffusive transport limitations through the boundary layer; thus, the final result is  $\gamma_{CN}(1273 \text{ K}) = (3.2 \pm 1.5) \times 10^{-3}$ .

Figures 8a and 8b show scanning electron micrographs of sample surfaces before and after nitridation at 1273 K. After testing, the sample surface shows clear evidence of mass loss through the formation of pits and an overall roughening of the surface. The nitridation reaction appears to preferentially occur at select locations on the surface. This preference may be related to intergrain carbon phases that are less strongly bonded or to the orientation of individual, highly anisotropic graphite grains intersecting the surface. The characteristic surface roughness scale increases from about a  $\sim 1 \mu\text{m}$  to a 5–10  $\mu\text{m}$  level after testing. We did not find significant variations of sample roughness and general surface morphology with the distance from sample tip.

The selectivity of the surface reaction locations and the roughening of the graphite surface (i.e., the increase in the effective surface area) may be expected to cause some discrepancies between experimental measurements performed using different carbon or graphite materials. In addition, if the increase in surface roughness during nitridation affects the reaction rate significantly, it is expected that the derived effective reaction efficiency depends on the nitridation time. Furthermore, repeated nitridation treatments of the same sample should yield systematically increasing values of  $\gamma_{CN}$ , given the higher sample roughness at the beginning of consecutive treatments. Therefore, we performed several tests in which the same sample was nitridated repeatedly (2–3 times) under the nominally identical conditions. We found no systematic increase in  $\gamma_{CN}$  with repeated treatments, indicating that the effect of increasing roughness is insignificant within the present experimental uncertainties.

## B. Experiments at Other Temperatures

Additional experiments were carried out at other temperatures, listed in Table 3. Because Park and Bogdanoff [16] reported a large carbon nitridation efficiency of 0.3 even at room temperature, we conducted a test with the furnace off. For this test, the  $\text{N}_2$  flow rate

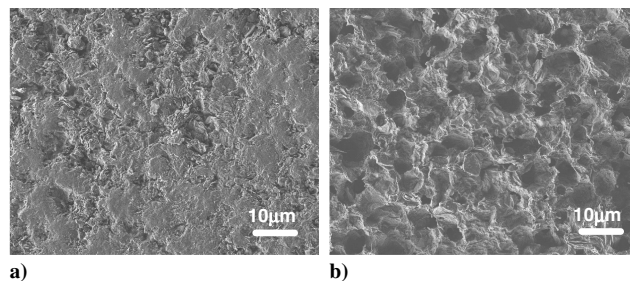


**Fig. 8** Scanning electron micrographs of the POCO DFP-2 graphite sample surfaces a) before and b) after N-atom nitridation at 1273 K (test ID G-1-11b).

**Table 3** Flow conditions for experiments conducted at different temperatures and a velocity of  $\sim 28.3 \text{ ms}^{-1}$ 

Test ID	$T_F$	$\dot{m}_{\text{N}_2, \text{in}}$	$P_1$	$P_2$	$P_s$	$\chi_{\text{N},1}$	$\chi_{\text{N},2}$	$C_{\text{N}}, 10^{-4} \text{ mol m}^{-3}$		
	K	$\text{mg s}^{-1}$	Pa	Pa	Pa	%	%	Max	Best	Min
O-2-28	873	10.4	266.0	213.3	249.3	0.225	0.059	0.772	0.372	0.201
P-2-30	873	20.0	499.6	446.6	482.8	0.180	0.086	1.198	0.798	0.571
Q-2-29	1073	10.2	320.0	263.3	302.0	0.273	0.117	0.923	0.567	0.395
Q-2-32	1073	10.2	320.0	263.3	302.0	0.273	0.117	0.923	0.567	0.395
R-2-33	1073	17.5	533.3	474.9	515.0	0.281	0.112	1.625	0.979	0.646
S-2-40	1173	7.7	266.6	207.3	248.1	0.243	0.120	0.618	0.407	0.306
T-2-41	1173	15.0	506.6	442.6	488.0	0.290	0.099	1.449	0.795	0.493
I-2-36	1273	10.4	386.6	324.0	366.2	0.352	0.128	1.227	0.703	0.445
I-2-54	1273	10.4	386.6	322.1	366.2	0.352	0.128	1.227	0.703	0.445
U-2-55	1373	6.5	266.6	201.3	246.4	0.231	0.046	0.499	0.204	0.100
V-2-56	1373	13.2	520.0	451.8	499.4	0.389	0.066	1.700	0.626	0.287

was  $15 \text{ mg s}^{-1}$  and the upstream pressure was 263 Pa. After 530 min of exposure time, we found a mass loss of only 0.03 mg which is near the resolution of our analytic balance. This mass loss yields a GK reaction efficiency of  $\sim 4 \times 10^{-6}$ , approximately 5 orders of magnitude lower than reported by Park and Bogdanoff [16].

We also conducted test series at 873, 1073, 1173, 1273, and 1373 K in which we attempted to maintain a constant bulk velocity around  $28.3 \text{ ms}^{-1}$  at the test specimen. These tests were performed using tube 2. The flow conditions and results are listed in Tables 3 and 4. Unlike Park and Bogdanoff [16], we find that  $\gamma_{\text{CN}}$  is not temperature independent, but increases as the temperature rises. The reaction efficiency at 873 K was about one order of magnitude lower than at 1273 K and the reaction efficiency at 1373 K was 4 to 5 times higher than those at 1273 K.

### C. Experiments with Molecular and Atomic Oxygen

Additional experiments were conducted to compare the derived nitridation rates to active oxidation rates for molecular and atomic oxygen with the same apparatus and under similar experimental conditions. These experiments are important because they provide a direct comparison of the relative efficiencies for carbon nitridation and oxidation.

In the first set of experiments, flow conditions were repeated with the discharge off and with  $\text{O}_2$  added at the first titration port at a volumetric flow rate similar to the N-atom volumetric flow rate during nitridation testing. This procedure roughly replaces the N-atom concentration at the sample location with an  $\text{O}_2$  concentration of similar magnitude. Since no  $\text{O}_2$  is lost by wall or gas-phase reactions, the  $\text{O}_2$  concentration at the sample location was calculated from the known mole fraction at the titration port, the furnace temperature, and the pressure at the sample location calculated from Eq. (3). We presume that CO, not  $\text{CO}_2$ , is the dominant product of oxidation with molecular oxygen. The efficiency for the  $\text{O}_2 + 2\text{C}_{(s)} \rightarrow 2\text{CO}$  surface reaction,  $\gamma_{\text{CO}}^{\text{O}_2}$ , can then be determined from the measured carbon mass loss by the same methods as the N-atom nitridation reaction efficiency.

In the second set of experiments, flow conditions were repeated with the discharge activated and the  $\text{N}_2/\text{N}$  flow was titrated with NO to approximately half of the previously determined endpoint. This procedure sets up roughly similar N-atom and O-atom concentrations at the sample location. The N-atom concentrations at the sample were interpolated using the reactive-flow model with previously determined values of the wall recombination efficiency. The concentration of O atoms at the sample was interpolated in the same way assuming the same wall recombination efficiency and gas-phase recombination rate coefficient as for N atoms. To evaluate the efficiency for the  $\text{O} + \text{C}_{(s)} \rightarrow \text{CO}$  surface reaction,  $\gamma_{\text{CO}}^{\text{O}}$ , we fixed  $\gamma_{\text{CN}}$  at its previously determined value under the same flow conditions and solved for the value of  $\gamma_{\text{CO}}^{\text{O}}$  that reproduces the measured mass loss. This procedure presumes that the  $\text{O} + \text{C}_{(s)} \rightarrow \text{CO}$  and  $\text{N} + \text{C}_{(s)} \rightarrow \text{CN}$  reactions operate in parallel and independently. The necessary diffusion coefficients and equilibrium constants for both types of oxidation experiments were obtained using the same methods and data sources as for the nitridation analyses.

Tables 5 and 6 give the flow conditions and the experimental results for the  $\text{O}_2$  experiments. Comparison of  $\gamma_{\text{CO}}^{\text{O}_2}$  in Table 6 with  $\gamma_{\text{CN}}$  in Table 4 at the same temperature, shows that the  $\text{O}_2 + 2\text{C}_{(s)} \rightarrow 2\text{CO}$  reaction is about an order of magnitude more efficient than the  $\text{N} + \text{C}_{(s)} \rightarrow \text{CN}$  reaction at 1073 and 1173 K and about a factor of 4 more efficient at 1273 K. At 873 K, the N-atom nitridation reaction is about an order of magnitude faster than the oxidation reaction, and at 1373 K the rates are comparable.

The flow conditions and experimental results for the O-atom experiments are given in Tables 7 and 8. The reaction efficiencies for the O-atom oxidation of graphite far exceed those for N-atom nitridation, by at least one and often 2 orders of magnitude, at all test temperatures in the 873–1273 K temperature range. The O-atom oxidation efficiency also exceeds the  $\text{O}_2$  oxidation efficiency, particularly at lower temperatures, a result that has been documented previously in the literature [4,35]. Because of this large reaction efficiency, the limiting effect of O-atom transport to the graphite surface is much more significant than in the case of the N-atom or  $\text{O}_2$

**Table 4** Mass loss data and computed reaction efficiencies for the flow conditions listed in Table 3

Test ID	$\Delta t$	$m_0$	$\Delta m_{\text{C,tot}}$	$\Delta m_{\text{C,con}}$	$L_s$	$\gamma_{\text{CN,GK}}, 10^{-3}$			$\gamma_{\text{CN,LBL}}, 10^{-3}$		
	min	mg	mg	mg	mm	Max	Best	Min	Max	Best	Min
O-2-28	360	547.74	0.41	0.09	29.8	0.70	0.38	0.18	0.73	0.40	0.19
P-2-30	327	550.22	0.33	0.16	29.0	0.15	0.11	0.07	0.15	0.11	0.07
Q-2-29	300	558.11	0.61	0.10	29.6	0.62	0.43	0.27	0.65	0.45	0.28
Q-2-32	280	555.65	0.58	0.09	29.7	0.64	0.44	0.27	0.67	0.46	0.28
R-2-33	305	552.91	0.45	0.15	29.5	0.22	0.15	0.09	0.23	0.15	0.09
S-2-40	253	544.89	0.63	0.07	30.0	0.98	0.74	0.49	1.03	0.78	0.51
T-2-41	319	618.76	1.59	0.17	35.0	1.06	0.65	0.36	1.12	0.70	0.38
I-2-36	180	545.21	1.58	0.06	30.0	2.47	1.57	0.90	2.74	1.73	0.89
I-2-54	174	581.53	2.15	0.06	31.2	3.39	2.14	1.23	3.86	2.44	1.22
U-2-55	133	507.71	2.04	0.03	28.0	20.3	9.95	4.07	32.0	15.8	6.45
V-2-56	114	554.39	3.99	0.06	30.2	15.0	6.87	2.53	24.0	11.0	4.06

**Table 5** Flow conditions for O<sub>2</sub> experiments; velocity of  $\sim 28.3$  ms<sup>-1</sup>

Test ID	$T_F$ K	$\dot{m}_{N_2,in}$ mg s <sup>-1</sup>	$\dot{m}_{O_2,in}$ mg s <sup>-1</sup>	$P_1$ Pa	$P_2$ Pa	$P_s$ Pa	$\chi_{O_2}$ %	$C_{O_2}$ 10 <sup>-4</sup> mol m <sup>-3</sup>
O-2-51-O <sub>2</sub>	873	10.4	0.026	266.6	211.6	250.2	0.220	0.756
Q-2-50-O <sub>2</sub>	1073	10.2	0.032	320.0	260.4	302.1	0.275	0.929
S-2-49-O <sub>2</sub>	1173	7.7	0.021	266.6	204.9	248.0	0.243	0.617
S-2-52-O <sub>2</sub>	1173	7.7	0.021	266.6	204.4	248.0	0.243	0.617
S-2-60-O <sub>2</sub>	1173	7.7	0.024	266.6	204.6	248.0	0.270	0.685
I-2-48-O <sub>2</sub>	1273	10.4	0.042	386.6	321.3	367.2	0.351	1.214
H-2-53-O <sub>2</sub>	1273	7.1	0.019	266.6	201.3	247.3	0.229	0.535
U-2-58-O <sub>2</sub>	1373	6.5	0.017	266.6	201.3	246.6	0.233	0.503
U-2-59-O <sub>2</sub>	1373	6.5	0.030	266.6	201.3	246.6	0.399	0.860

**Table 6** Mass loss data and computed reaction efficiencies for the flow conditions listed in Table 5

Test ID	$\Delta t$ min	$m_0$ mg	$\Delta m_{C,tot}$ mg	$\Delta m_{C,con}$ mg	$L_s$ mm	$\gamma_{CO,GK}^{O_2}$ 10 <sup>-3</sup>	$\gamma_{CO,LBL}^{O_2}$ 10 <sup>-3</sup>
O-2-51-O <sub>2</sub>	225	568.49	0.09	0.04	30.5	0.034	0.036
Q-2-50-O <sub>2</sub>	153	565.87	5.54	0.09	31.0	3.97	4.73
S-2-49-O <sub>2</sub>	222	540.12	12.71	0.06	30.0	9.48	14.0
S-2-52-O <sub>2</sub>	105	516.72	5.72	0.03	29.0	9.32	13.0
S-2-60-O <sub>2</sub>	64	548.26	3.32	0.02	31.0	7.48	9.90
I-2-48-O <sub>2</sub>	125	559.00	7.45	0.04	30.7	4.71	5.80
H-2-53-O <sub>2</sub>	116	517.36	5.03	0.03	28.5	8.35	11.0
U-2-58-O <sub>2</sub>	59	488.13	1.50	0.02	26.7	5.30	6.33
U-2-59-O <sub>2</sub>	113	545.86	6.21	0.03	30.2	6.00	7.37

surface reactions. Unfortunately, the series summation in the LBL solution converges very slowly for large reaction efficiencies and we were not able to obtain converged solutions that reproduced the measured carbon mass loss. Therefore, only the GK reaction efficiency values are listed in Table 8. It is likely, however, that with transport limitations properly accounted for, the value of reaction efficiency would be higher.

## V. Discussion

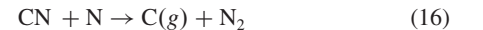
The GK reaction efficiencies for the three investigated reactive species are compared in Fig. 9. It is evident that none of the reactions follow simple Arrhenius behavior (i.e., a single, constant activation energy) over the temperature range of our experiments. Our O<sub>2</sub> oxidation results are similar to the measurements of Rosner and Allendorf [35] in that the reaction probability rises rapidly with increasing temperature, but then passes through maximum after which it decreases with increasing temperature. Like Rosner and Allendorf [35] we always find significantly higher reaction efficiencies for O atom than O<sub>2</sub> oxidation at the same temperature [35].

Comparisons of our numerical values for  $\gamma_{CO}^{O_2}$  and  $\gamma_{CO}^{O}$  with those of Rosner and Allendorf [35], as well as those computed from empirical relationships presented by Park [4], generally yield an order-of-magnitude level agreement. Given the experimental and data analysis complexities, the large variations in O<sub>2</sub> carbon oxidation data reported in the literature (see, e.g., Fig. 1 in Park's work [4]) and the large range reactivity exhibited by different types of

carbon in plasma environments [36], perhaps no closer agreement should be expected. The more important conclusion is that our technique obtains relative reaction efficiencies for carbon oxidation by O atoms and O<sub>2</sub> that are consistent with previously reported experiments. Since our N-atom, O-atom, and O<sub>2</sub> experiments are all conducted under similar flow conditions and reactant concentrations, and since the diffusion coefficients for O and N in molecular nitrogen are very similar, our result that N-atom nitridation is 1–2 orders of magnitude less efficient than O-atom oxidation is very robust.

The experimental data for  $\gamma_{CN}$  generated by Goldstein [15], Park and Bagdanoff [16], Suzuki et al. [18,20], and our current study are plotted together in Fig. 10. The majority of our measurements were obtained at 1273 K; the average value for these is about  $3 \times 10^{-3}$ . This average is very similar to the reaction efficiencies reported by Suzuki et al. [18,20] for their ICP graphite ablation experiments and is the value that produces the best agreement between experiment and modeling of those experiments [21]. Compared with our test conditions, most of their ICP experiments were conducted at higher temperatures (1822–2184 K), higher total pressure ( $\sim 10$  kPa), and much higher N-atom concentrations (by 2–3 orders of magnitude). Our 1273 K value of  $\gamma_{CN}$  is also similar to, although slightly larger than, the results published by Goldstein [15], who worked at higher temperatures but similar total pressure and atom concentrations as in our experiments. Despite the different experimental approaches taken, the different temperature ranges explored, and the different graphite materials used, these three studies yield comparable values of  $\gamma_{CN}$ . Whereas the data of Suzuki et al. [18,20] show weak temperature dependence, the experiments of Goldstein [15] indicate significant increase of the reaction efficiency with temperature. Our data also show the nitridation efficiency to increase with temperature, faster than in Goldstein's data and over a lower temperature range.

The values of  $\gamma_{CN}$  reported by Park and Bagdanoff [16] are about 2 orders of magnitude higher than the values reported by other researchers and the origin of this discrepancy is at present not understood. As pointed out by Suzuki et al. [18,19], low carbon mass losses observed in nitridation experiments can, in principle, be reconciled with high values of  $\gamma_{CN}$  if significant carbon recondensation occurs. Carbon atoms removed from sample by nitridation are partly recovered in the gas phase by the reaction



which has a recommended rate coefficient of  $3 \times 10^{-10}$  cm<sup>3</sup> molecule<sup>-1</sup> s<sup>-1</sup> between 300 and 2500 K [37]. Some regenerated carbon atoms may recondense on the sample surface,

**Table 7** Flow conditions for O-atom experiments; velocity of  $\sim 28.3$  ms<sup>-1</sup>

Test ID	$T_F$ K	$\dot{m}_{N_2,in}$ mg s <sup>-1</sup>	$\dot{m}_{NO,in}$ mg s <sup>-1</sup>	$P_1$ Pa	$P_2$ Pa	$P_s$ Pa	$C_O$ 10 <sup>-4</sup> mol m <sup>-3</sup>	$C_N$ 10 <sup>-4</sup> mol m <sup>-3</sup>
O-2-45-O	873	10.4	0.0125	266.6	210.9	250.1	0.184	0.185
Q-2-43-O	1073	10.2	0.0150	320.0	258.6	302.0	0.284	0.283
Q-2-44-O	1073	10.2	0.0150	320.0	258.6	302.0	0.284	0.283
S-2-47-O	1173	7.7	0.0107	266.6	204.6	248.0	0.204	0.204
I-2-46-O	1273	10.4	0.0194	386.6	326.0	368.0	0.339	0.349
U-2-57-O	1373	6.5	0.0085	266.6	201.5	246.6	0.102	0.102

**Table 8** Mass loss data and computed reaction efficiencies for the flow conditions listed in Table 7

Test ID	$\Delta t$ min	$m_0$ mg	$\Delta m_{C,tot}$ mg	$\Delta m_{C,con}$ mg	$L_s$ mm	$\gamma_{CO,GK}^O$ $10^{-3}$
O-2-45-O	177	547.07	15.62	0.03	29.9	80
Q-2-43-O	256	550.94	31.93	0.14	29.3	68
Q-2-44-O	175	558.55	21.94	0.10	31.0	64
S-2-47-O	128	554.93	14.08	0.04	30.2	77
I-2-46-O	81	553.75	17.84	0.03	30.8	86
U-2-57-O	59	546.57	7.36	0.02	30.2	152



effectively reducing the net carbon mass loss. The extent of carbon recondensation depends on the carbon-carbon sticking coefficient and specific experimental parameters that determine the residence times and concentrations of reactants near the sample surface: notably, flow speed and pressure. An assessment of the possible effects of processes (16) and (17) on the values of  $\gamma_{CN}$  derived from our experimental data requires detailed CFD modeling of the experiment that includes the actual sample-holder geometry, all relevant gas-phase reactions and transport models, and point-by-point coupling between the reactive boundary-layer flow and finite rate surface reactions on the graphite surface. Although such a modeling effort is beyond the scope of the present study, we note that the experiments and results have been described in great detail,

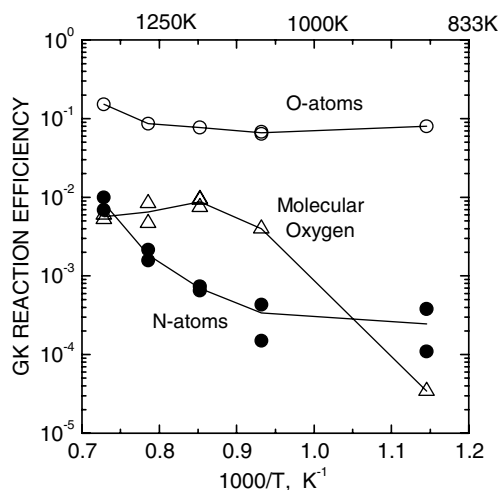


**Fig. 9** GK reaction efficiencies versus inverse temperature; where more than one data point is available at a given temperature, the lines connect the average values.

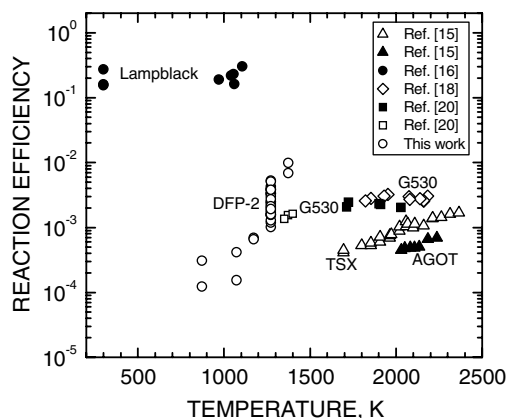


**Fig. 10** Reaction efficiency for carbon active nitridation by N atoms as determined by different investigators.

specifically to enable more extensive modeling and analysis by interested researchers with the necessary computational tools.

On a qualitative level, the effects of carbon recondensation could be observable as differences in the surface morphology between the parts of the graphite sample near the tip and near the sample holder, given that the sample surface further downstream is potentially exposed to more extensive recondensation. As noted in Sec. IV.A, SEM imaging did not show significant differences in the sample surface morphology with varying the distance from the tip; therefore, there are no clear indications of recondensation on our samples, although it cannot be excluded.

Surface recession is a major issue in the design of TPS materials. Based on the relatively low values of  $\gamma_{CN}$  reported here and, more directly, the low rate of sample mass losses, nitridation by N atoms is not likely to drive significant recession of carbon-based TPS materials below 1373 K, especially in air environments where mass loss through oxidation is expected to dominate. However, given that we find that  $\gamma_{CN}$  increases rapidly with temperature, more significant mass loss due to N-atom nitridation is possible at temperatures exceeding 1373 K.

## VI. Conclusions

We have found a very small carbon loss by N-atom nitridation near room temperature, implying that the reaction efficiency must be lower than  $10^{-5}$  under these conditions and our experiments suggest a reaction efficiency at least 100 times smaller at 1100 K than that reported by Park and Bogdanoff [16]. We have also demonstrated that the active nitridation efficiency of DFP-2 graphite is much lower than that of O-atom oxidation over the 873–1373 K temperature range. The reaction efficiencies that we measured in a flow tube system are similar in magnitude to previously published results by Goldstein [15] and Suzuki et al. [18,20] measured using other techniques and show an increasing reaction efficiency with increasing temperature.

## Acknowledgment

This work was supported by NASA grant NNX08AC98A.

## References

- [1] Laub, B., and Venkatapathy, E., "Thermal Protection System Technology and Facility Needs for Demanding Future Planetary Missions," *Planetary Probe Atmospheric Entry and Descent Trajectory Analysis and Science*, ESA SP-544, edited by A. Wilson, ESA, Noordwijk, The Netherlands, 2004, pp. 239–247.
- [2] Chen, Y.-K., and Milos, F. S., "Navier-Stokes Solutions with Finite Rate Ablation for Planetary Mission Earth Reentries," *Journal of Spacecraft and Rockets*, Vol. 42, No. 6, 2005, pp. 961–970. doi:10.2514/1.12248
- [3] Kendall, R. M., Bartlett, E. P., Rindal, R. A., and Moyer, C. B., "An Analysis of the Coupled Chemically Reacting Boundary Layer and Charring Ablator, Part I. Summary Report," NASA CR-1060, June 1968.
- [4] Park, C., "Effects of Atomic Oxygen on Graphite Ablation," *AIAA Journal*, Vol. 14, 1976, pp. 1640–1642. doi:10.2514/3.7267
- [5] Park, C., and Ahn, H.-K., "Stagnation-Point Heat Transfer Rates for Pioneer-Venus Probes," *Journal of Thermophysics and Heat Transfer*, Vol. 13, No. 1, 1999, pp. 33–41. doi:10.2514/2.6426
- [6] Suzuki, T., Furudate, M., and Sawada, K., "Unified Calculation of Hypersonic Flowfield for a Reentry Vehicle," *Journal of Thermophysics and Heat Transfer*, Vol. 16, No. 1, 2002, pp. 94–100. doi:10.2514/2.6656
- [7] Zhuktov, S. V., and Abe, T., "Viscous Shock-Layer Simulation of Airflow Past Ablating Blunt Body with Carbon Surface," *Journal of Thermophysics and Heat Transfer*, Vol. 13, No. 1, 1999, pp. 50–59. doi:10.2514/2.6400
- [8] Havstad, M. A., and Ferencz, R. M., "Comparison of Surface Chemical Kinetic Models for Ablative Reentry of Graphite," *Journal of Thermophysics and Heat Transfer*, Vol. 16, No. 4, 2002, pp. 508–515. doi:10.2514/2.6725
- [9] Chen, Y.-K., and Milos, F. S., "Finite Rate Ablation Boundary

- Conditions for a Carbon-Phenolic Heat-Shield," AIAA Paper 2004-2270, June 2004.
- [10] Beerman, A. F., Lewis, M. J., Starkey, R. P., and Cybyk, B. Z., "Nonequilibrium Surface Interactions Ablation Modeling with the Fully Implicit Ablation and Thermal Response Program," AIAA Paper 2008-1224, Jan. 2008.
- [11] Park, C., Raiche, G. A., and Driver, D. M., "Radiation of Spalled Particles in Shock Layers," *Journal of Thermophysics and Heat Transfer*, Vol. 18, No. 4, 2004, pp. 519–526.  
doi:10.2514/1.8098
- [12] Vancraynest, B., and Fletcher, D. G., "Ablation of Carbonaceous Heatshields: Spectroscopic Emission Survey in a Subsonic ICP Flow," AIAA Paper 2008-3911, June 2008.
- [13] Vancraynest, B., and Fletcher, D. G., "Emission Spectroscopy Survey of Graphite Ablation in the VKI Plasmatron," AIAA Paper 2006-2907, June 2006.
- [14] Park, C., Jaffe, R. L., and Partridge, H., "Chemical-Kinetic Parameters of Hyperbolic Earth Entry," *Journal of Thermophysics and Heat Transfer*, Vol. 15, No. 1, 2001, pp. 76–90.  
doi:10.2514/2.6582
- [15] Goldstein, H. W., "The Reaction of Active Nitrogen with Graphite," *Journal of Physical Chemistry*, Vol. 68, No. 1, 1964, pp. 39–42.  
doi:10.1021/j100783a007
- [16] Park, C., and Bogdanoff, D. W., "Shock-Tube Measurement of Nitridation Coefficient of Solid Carbon," *Journal of Thermophysics and Heat Transfer*, Vol. 20, No. 3, 2006, pp. 487–492.  
doi:10.2514/1.15743
- [17] Whiting, E. E., Park, C., Liu, Y., Arnold, J. O., and Paterson, J. A., "NEQAIR96 Nonequilibrium and Equilibrium Radiative Transport and Spectra Program: User's Manual," NASA Ref. Pub. 1389, Dec. 1996.
- [18] Suzuki, T., Fujita, K., Ando, K., and Sakai, T., "Experimental Study of Graphite Ablation in Nitrogen Flow," *Journal of Thermophysics and Heat Transfer*, Vol. 22, No. 3, 2008, pp. 382–389.  
doi:10.2514/1.35082
- [19] Suzuki, T., Fujita, K., and Sakai, T., "Numerical Analysis of Graphite Ablation in Nitrogen," AIAA Paper 2008-1217, Jan. 2008.
- [20] Suzuki, T., Fujita, K., and Sakai, T., "Graphite Nitridation in Lower Surface Temperature Regime," *Journal of Thermophysics and Heat Transfer*, Vol. 24, No. 1, 2010, pp. 212–215.  
doi:10.2514/1.43265
- [21] Suzuki, T., Fujita, K., and Sakai, T., "Experimental Study of Graphite Ablation in Nitrogen Flow, Part II: Further Numerical Analysis," *Journal of Thermophysics and Heat Transfer*, Vol. 24, No. 3, 2010, pp. 589–597.  
doi:10.2514/1.43264
- [22] Sander, S. P., Friedl, R. R., Golden, D. M., Kurylo, M. J., Moortgat, G. K., Wine, P. H., et al., "Chemical Kinetics and Photochemical Data for Use in Atmospheric Studies: Evaluation Number 15," Jet Propulsion Lab., Rept. 06-2, Pasadena, CA, July 10 2006.
- [23] Sutoh, M., Morioka, Y., and Nakamura, M., "Absolute Rate Constant for the Chemiluminescent Reaction of Atomic Oxygen with Nitric Oxide," *Journal of Chemical Physics*, Vol. 72, No. 1, 1980, pp. 20–24.  
doi:10.1063/1.438878
- [24] Touloukian, Y. S., Saxena, S. C., and Hestermans, P., *Thermophysical Properties of Matter—Viscosity*, Vol. 11, IFI/Plenum, New York, 1975.
- [25] Kim, Y. C., and Boudart, M., "Recombination of O, N, and H Atoms on Silica: Kinetics and Mechanism," *Langmuir*, Vol. 7, No. 12, 1991, pp. 2999–3005.  
doi:10.1021/la00060a016
- [26] Marschall, J., "Experimental Determination of Oxygen and Nitrogen Recombination Coefficients at Elevated Temperature Using Laser-Induced Fluorescence," AIAA Paper 97-3879, Aug. 1997.
- [27] Marshall, T., "Surface Recombination of Nitrogen Atoms Upon Quartz," *Journal of Chemical Physics*, Vol. 37, 1962, pp. 2501–2502.  
doi:10.1063/1.1733039
- [28] Rahman, M. L., and Linnett, J. W., "Recombination of Atoms at Surfaces, part 10—Nitrogen Atoms at Pyrex Surfaces," *Transactions of the Faraday Society*, Vol. 67, 1971, pp. 170–178.  
doi:10.1039/tf9716700170
- [29] Baulch, D. L., Drysdale, D. D., and Horne, D. G., *Evaluated Kinetic Data for High Temperature Reactions, Volume 2: Homogeneous Gas Phase Reactions of the H<sub>2</sub>-N<sub>2</sub>-O<sub>2</sub> System*, Butterworths, London, 1973.
- [30] Acrivos, A., and Chambré, P. L., "Laminar Boundary Layer Flows with Surface Reactions," *Industrial and Engineering Chemistry*, Vol. 49, No. 6, 1957, pp. 1025–1029.  
doi:10.1021/ie50570a037
- [31] Wright, M. J., Bose, D., Palmer, G. E., and Levine, E., "Recommended Collision Integrals for Transport Property Computations, Part 1: Air Species," *AIAA Journal*, Vol. 43, No. 12, 2005, pp. 2558–2564.  
doi:10.2514/1.16713
- [32] Wright, M. J., Hwang, H. H., and Schwenke, D. W., "Recommended Collision Integrals for Transport Property Computations Part 2: Mars and Venus Entries," *AIAA Journal*, Vol. 45, No. 1, 2007, pp. 281–288.  
doi:10.2514/1.24523
- [33] Roine, A., *HSC Chemistry for Windows, Version 5.11*, Outokumpu Research Oy, Pori, Finland, 2006.
- [34] Gaskell, D. R., *An Introduction to Transport Phenomena in Materials Engineering*, Macmillan, New York, 1992.
- [35] Rosner, D. E., and Allendorf, H. D., "Comparative Studies of the Attack of Pyrolytic and Isotropic Graphite by Atomic and Molecular Oxygen at High temperatures," *AIAA Journal*, Vol. 6, 1968, pp. 650–654.  
doi:10.2514/3.4558
- [36] Cuesta, A., Martínez-Alonso, A., and Tascón, J. M. D., "Carbon Reactivity in an Oxygen Plasma: A Comparison with Reactivity in Molecular Oxygen," *Carbon*, Vol. 39, 2001, pp. 1135–1146.  
doi:10.1016/S0008-6223(00)00235-9
- [37] Baulch, D. L., Cobos, C. J., Cox, R. A., Esser, C., Frank, P., Just, T., et al., "Evaluated Kinetic Data for Combustion Modelling," *Journal of Physical and Chemical Reference Data*, Vol. 21, 1992, pp. 411–429.  
doi:10.1063/1.555908

## Queries

### **IMPORTANT: PLEASE READ CAREFULLY.**

When production of AIAA journal papers begins, the official approved PDF is considered the authoritative manuscript. Authors are asked to submit source files that match the PDF exactly, to ensure that the final published article is the version that was reviewed and accepted by the associate editor. Once a paper has been accepted, any substantial corrections or changes must be approved by the associate editor before they can be incorporated.

If you and the EIC settled on some final changes to your manuscript after it was accepted, it is possible that your page proofs do not reflect these final changes. If that is the case, please submit these changes as itemized corrections to the proofs.

If final changes were made to the figures, please check the figures appearing in the proofs carefully. While it is usual procedure to use the figures that exist in the source file, if discrepancies are found between figures (manuscript source file vs the approved PDF), the figures from the PDF are inserted in the page proofs, again deferring to the PDF as the authoritative manuscript. If you find that agreed-upon final changes to your figures are not appearing in your page proofs, please let us know immediately.

- Q1.** Is the above © information (type A copyright) correct?
- Q2.** Please provide a new Conclusions paragraph that avoids first-person voice and citations of any kind, which are all now prohibited in the Conclusions.